Evolution of Microstructure and Surface Characteristics of FeCrAl alloys when Subjected to Flow Boiling Testing

Rajnikant V. Umretiya[1], Donghwi Lee[2], Barret Elward[2], Mark Anderson[2], Raul B. Rebak[3], Jessika V. Rojas*[1]

[1]*Department of Mechanical and Nuclear Engineering, Virginia Commonwealth University, Richmond, VA, 23284, USA*

[2]*Department of Mechanical Engineering, University of Wisconsin-Madison, Madison, WI, 53706, USA*

[3]*GE Research, Schenectady, NY, 12309, USA*

* Corresponding Author: jvrojas@vcu.edu; Phone: (804)828-4267.

ABSTRACT

FeCrAl alloys are candidate materials for manufacturing accident-tolerant fuel (ATF) cladding intended for light water reactors to increase fuel reliability and safety during design-basis and beyond-design-basis accident scenarios. The evolution of the materials' surface characteristics, microstructure, and mechanical properties when exposed to the Critical Heat Flux (CHF) in flow boiling testing is crucial for safety analysis while providing insights into their thermal-hydraulic performance in nuclear reactors. After CHF, the surface chemistry of two FeCrAl alloys, APMT and C26M, was studied to understand their evolution at the early stage of high-temperature excursions in short time periods. The results indicated a thin layer composed of oxides and hydroxides of Al, Cr, and Fe with varying proportions at different depths in the layer, as indicated by X-ray photoelectron spectroscopy (XPS) and depth profiling. The cross-sections prepared by focused ion beam (FIB) revealed the growth of an oxide layer, in the range of 90-180 nm thick, on the alloys' surfaces. The evolution of the materials' surface chemistry also led to a noticeable post CHF excursion increase in their wettability, with a slight increase in roughness. The investigation of the materials' mechanical properties indicated a modest increase in hardness by 10-15% as well as an increase in their yield strength, as evidenced by the microindentation and ring compression tests conducted before and after CHF testing. Scanning electron Microscopy (SEM) and X-ray diffraction (XRD) were used to investigate microstructural features of the materials and their changes after CHF treatment.

Keywords: Accident tolerant fuel, ATF, FeCrAl alloys, APMT, C26M, Critical heat flux (CHF), surface chemistry, wettability.

1. Introduction

In nuclear power generation, all light water reactors (LWRs) are designed with safety features and protocols to withstand design-basis and beyond design accidents and to guarantee that the reactor core is provided with adequate cooling to avoid a meltdown. However, in 2011, the Fukushima accident highlighted the weakness of standard Zircaloy cladding and the need for developing new strategies to improve the ability of LWRs systems to react to accidents and maintain the integrity of the core [1][2]. As a result, one of the many approaches considered by the nuclear community is developing new fuel technologies with superior oxidation resistance at high temperatures [3]. The main focus while designing the new nuclear fuel claddings, known as accident tolerant fuels (ATF), is to reduce or eliminate hydrogen generation under high temperatures typical of accident conditions, thus providing more coping time to take actions that prevent or otherwise alleviate system damage [4][5]. The high-temperature steam oxidation resistance is considered a key factor among the requirements for ATF cladding candidate materials, such as high thermal and mechanical performance and high irradiation stability [6]. Materials that form protective oxide layers of chromium, alumina, or silica are far more resistant than Zircaloy to high-temperature steam oxidation; thus, they may fulfill the requirements set forth for ATFs. These oxide layers limit the diffusion of oxidizing species, protecting the underlying material [2]. Many ATF cladding concepts, such as (a) coated Zircaloy [7][8], (b) coated Mo-alloy [9], (c) iron-based alloys [10], and (d) SiC_f/SiC composites [11][12] are in research/testing phase which can improve the performance of current Zr-based alloys.

Based on the designs and cladding concepts, ATF cladding materials can be distinguished into two different categories: near- and longer-term technologies [13]. To use existing infrastructure, experience, and expertise with traditional Zircaloy fuel cladding in LWRs to the maximum extent possible, the deposition of coatings on the current Zircaloy is a promising near-term ATF cladding concept. The advantages related to this approach include 1) well-known physical and chemical properties of the base material, 2) reduced fretting corrosion, and 3) minimized hydrogen release during loss-of-coolant accidents [14][15]. Thus, different protective coating materials and the deposition techniques [16][17][18][19][20][21][22][23][24][25][26] are under investigation in the development of coated ATF claddings. Among different possible coating materials considered for ATF claddings, chromium has shown favorable results [27][28][29][30][31][32][33]. Various studies have evidenced the improved mechanical and thermal performance of traditional Zircaloy cladding when coated with Cr. The studies include materials testing in humid environments at room temperature [34][35], simulated PWR operating conditions in autoclave, and high-temperature steam environments [7][36][37]. Cr-coatings have also

demonstrated good irradiation stability [38][39][40]. Furthermore, some studies in the literature have reported good adhesion strength of the coatings during the ring tensile and ring compression tests with improved mechanical properties than that of the substrate materials [34][41].

FeCrAl alloys as a lead ATF cladding candidates in near-term solutions have shown outstanding high-temperature oxidation resistance during various accident scenarios for LWRs [13][42][43][44][45][46][47]. The literature has evidenced the remarkable stability of microstructural and mechanical properties of FeCrAl alloys at different radiation doses [10][48][49]. Moreover, high ultimate tensile and yield strength are reported for unirradiated FeCrAl alloys at different temperatures [50][51][52][53]. To compensate the neutron penalty due to the higher thermal neutron absorption cross-section of FeCrAl alloys compared to that of Zircaloy, a thinner cladding with slightly higher enriched fuel can be used to maintain cycle length [13][52].

Despite the favorable properties of the ATF cladding concepts, investigating and understanding their thermal-hydraulic performance by measuring critical heat flux (CHF) and nucleate boiling heat transfer coefficients (NBHTC) is critical to enable their use in nuclear reactors [54][55][56]. The CHF occurs when the steam produced in the system replaces the liquid in contact with the heating surface, resulting in the transition from the nucleate boiling regime to the film-boiling regime [57]. As such, the surface temperature of cladding abruptly increases at CHF, compromising its structural integrity, and with the danger of radionuclide release into the coolant [57]. Therefore, accurate knowledge of the CHF value is essential to designing systems that involve two-phase heat transfer mechanisms. Due to the complexity of CHF, many empirical correlations have been developed based on experimental outcomes and theoretical reasoning [58][59][60][61][62]. Earlier CHF models such as Zuber CHF correlation [62] ignored the effects of the boiling surface characteristics; however, experimental results have evidenced the importance of the surface' physical and chemical characteristics, such as roughness, wettability, and thermal properties of the cladding on CHF [63][64][65][66][67][68][69][70] [71].

Given the high temperatures of the cladding expected at CHF, it becomes crucial to understand the materials' surface chemistry when this event occurs as it would provide the chemical nature of the oxides formed at the early stage. These studies would lead to knowledge of oxidation mechanisms and kinetics, ultimately explaining materials' performance. For example, Lee et. al. [72] repeated the flow boiling experiment several times using the same test specimens to study CHF enhancement due to the impact of evolving surface characteristics. After ten repetitions of this experiments, the average contact angle of FeCrAl, Zircaloy-4, and Inconel 600 decreased from pre-CHF samples contact angle of 69.43°, 76.48° and 73.79° to 53.64°, 64.04° and 55.92°, respectively. Similarly, a decrease in the surface roughness was evidenced in all the materials after flow boiling experiments. The changes in wettability and surface roughness of FeCrAl alloys and Zircaloy-4 surfaces could be attributed to the development of an oxide

layer [72][73]. In our previous work [34], a Zircaloy-4 substrate and two types of Cr-coated Zircaloy samples produced by physical vapor deposition (PVD) and cold spray (CS) techniques were tested in flow boiling test. This study evidenced changes in the wettability after testing due to the materials' surface evolution. Furthermore, the roughness was increased for all tested samples. Hence, this opens a research scope to study the surface properties of ATF materials and changes in surface chemistry when CHF is achieved.

In this study, we analyzed the surface characteristics and surface chemistry of FeCrAl alloys, namely APMT and C26M, pre- and post- flow boiling CHF testing conducted at atmospheric pressure. The surface roughness was quantitatively measured using contact profilometry and results were validated with qualitative data of atomic force microscopy (AFM). The surface wetting characteristics were assessed using contact angle goniometry. Furthermore, the materials' microstructure was studied using SEM and XRD. Finally, detailed surface chemistry analysis of the selected ATF materials, carried out by XPS, evidenced the growth of various oxides throughout the test. These results elucidate the rapid response of FeCrAl alloys toward accident scenarios.

2. Materials and Methods

2.1. Sample preparation

The FeCrAl samples used in this study, APMT, a commercial product of Kanthal®, and C26M is a nuclear grade alloy with reduced Cr content developed by ORNL. The tubes have a typical external diameter of 10.26 mm diameter, and a wall thickness of 0.40 mm. Table 1 shows the chemical compositions of the samples. Approximately 5 mm long specimens were cut out of the tubes using a low-speed saw (Buehler IsoMet) for characterization. A list of samples with their identification and descriptions is provided in Table 2. The specimens were cleaned in an ultrasonic bath for ~3 minutes using Alconox®, deionized (DI) water, and acetone in each step and dried in air. Finally, the specimens were embedded in epoxy resin (acquired from Allied Chemicals Inc) for post-test examinations followed by polishing.

Table 1. Chemical composition of FeCrAl alloys (as obtained from energy dispersive spectroscopy).

%wt.	Cr	Al	Mo	Y	Si	Fe
APMT	20.53	5.20	4.11	0.88	0.76	Balance
C26M	11.73	6.48	2.92	0.74	0.68	Balance

Table 2. Test sample identification (ID) with their description.

Sample ID	Conditions
APMT_Pre-CHF	As received APMT sample before flow boiling test
C26M_Pre-CHF	As received C26M sample before flow boiling test
APMT_Post-CHF	APMT sample tested in flow boiling CHF test
C26M_Post-CHF	C26M sample tested in flow boiling CHF test

2.2. Atmospheric pressure flow boiling CHF test

FeCrAl materials were tested to measure CHF under atmospheric pressure in a flow boiling facility (Fig. 1(a-b)). The details of the test facility at the University of Wisconsin-Madison Thermal Hydraulics Lab are provided in other studies published by the lab [74][75]. The uniform heat flux profile was obtained through direct heating (by applying current) of the FeCrAl heater rod. Table 3 shows the testing parameters used in this study. Inlet conditions of flow (listed in Table 3) were kept constant while the heat flux was increased by changing the applied voltage.

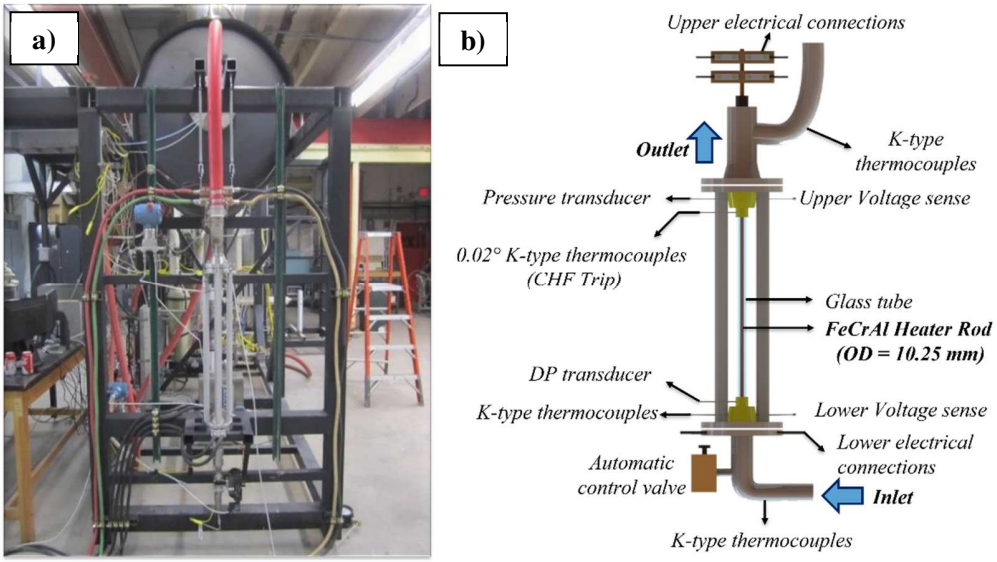

Fig. 1. CHF testing: a) Flow boiling atmospheric pressure test facility with b) test section (adapted from [74]**).**

The procedure for determining CHF was executed as follows [75]. The heat flux was manually raised from 0 to 2000 kW/m^2 (determined to be below the critical heat flux) by approximately 330 kW/m^2 every 2 minutes. The increments of ~330 kW/m^2 and 2 minutes were chosen to quickly reach near CHF conditions while allowing time to steady-state for the system. During this manual ramp, process data was

recorded at 2 Hz, and the temperature profile was recorded at 5 Hz. When the heat flux value reached 2000 kW/m^2, the heat flux was set to increase automatically every 10 s by 1.25 kW/m^2 until CHF was detected using the LabView process monitoring system (operating at 50 Hz). The detection of CHF was tripped using a rate of 50 Hz by 0.02 °C K-type thermocouples near the outlet (Fig. 1(b)), set at 20-25 °C above the steady-state temperature of the heater rod. The CHF critical temperature is typically in the range of 190-220 °C. The design of this facility allows automatic power cut off when CHF is detected to stop further heating of the heater rod, which could cause damage to the experimental setup. During CHF event, the LUNA system (distributed fiber temperature measurement) records the temperature of the heater rod for 10 seconds before and after CHF. As a backup CHF trip mechanism, the heater rod resistance deviation was also observed by 10 Hz to determine the CHF occurrence. The resistance threshold was purposefully set slightly above the observed operating resistance of the heater rod calculated from the measured voltage drop and applied current to the heater rod. This provided additional safety precautions if the CHF event was initiated far away from the thermocouple.

Table 3. Testing parameters used for the flow boiling CHF test.

Testing parameter	Value
Cladding material	FeCrAl alloys (APMT, and C26M)
Cladding tube OD (mm)	10.25
Cladding wall thickness (mm)	0.51
Working fluid	Water
Nominal heat flux (MW/m^2)	0 - 3
Inlet temperature (ºC)	24
Inlet pressure (kPa)	115
Nominal mass flux (kg/m^{2}s)	750
Heated length (mm)	457.2
Hydraulic diameter (mm)	9.8

2.3. Surface characterization

The specimens were measured at ambient conditions using a Rame-hart contact angle goniometer to acquire their static contact angle, providing quantitative information of their surface wettability. Fig. 2 shows an experimental setup for contact angle measurements along with an inset indicating a DI water droplet deposited on the surface. While measuring contact angle, the visualization direction needs to be identified because the water droplet has shown to behave differently along the different measuring directions, especially for surfaces with unidirectional scratches [59]. In this study, the visualization

direction was parallel to the surface scratches (Fig. 2). The device is connected to a high-speed camera (NET GmbH 1394 Digital Camera) and an automated dispensing system that allows for accurate control over the droplet volume, assuring measurement repeatability. The ASTM standards for contact angle measurements of metal surfaces provide a detailed measuring procedure [76]. A total of fifty measurements of the static contact angle were taken throughout the surface using a 5 μL drop of DI water to provide a representative value of the contact angle.

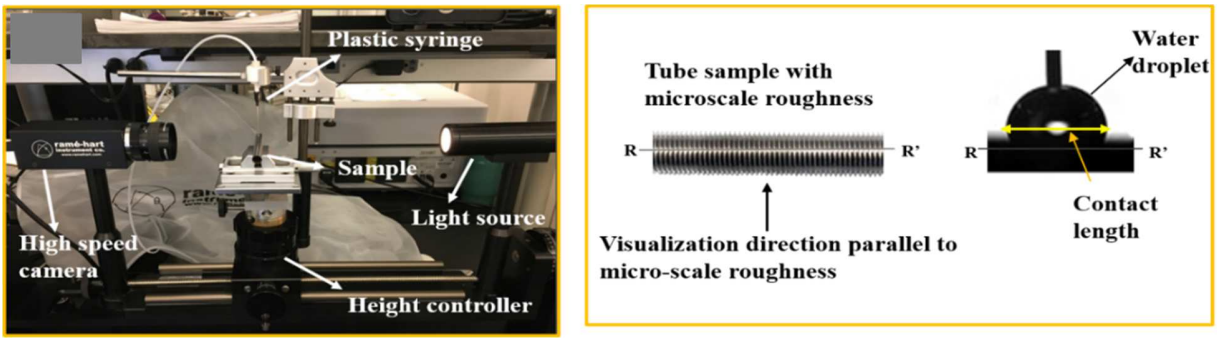

Fig. 2. Schematic of contact angle measurement device (adopted from our previous work [77]**).**

The surface profile of the specimens was measured with a stylus profilometer (Mitutoyo Surftest SJ-410), using a tip of 2 μm radius and 60° tip angle. The different roughness parameters such as, Ra, Rz, and RSm, were collected following ISO standards [78]. A total of fifty scans, each 5 mm long, were randomly collected throughout the surface from the various specimens with 0.5 mm/s scanning speed. Each profile was obtained by filtering with a Gauss filter using the cutoff length of 0.8 mm. AFM (Bruker Dimension Icon) operating in tapping mode was utilized with AFM tip TESPA-V2 (Bruker) to study the surfaces' topographies at the nanoscale. The microscope is capable of scanning up to an 8100 μm^2 scan area.

2.4. Surface chemistry

Surface chemistry analysis of FeCrAl samples was conducted before and after CHF testing using a PHI VersaProbe III XPS, equipped with a Al k-Alpha monochromatic X-ray source. The specimens were subjected to argon ion beam sputtering for depth-profiling analysis. During the etching, the beam energy and current were set to 3 keV and 1 μA, respectively. For depth profiling, a 9 mm^2 area over the specimen surface was scanned by the ion beam. Before data collection for FeCrAl samples, the beam current was calibrated using standard SiO_2 film of 250 Å thickness. Several high-resolution spectra of Al2p, Fe2p, and Cr2p were collected using 26 eV pass energy settings and calibrated with 284.8 eV binding energy of the

adventitious carbon C1s. The XPS data were analyzed in Casa XPS software (Version 2.3.19PR 1.0) with Gaussian/Lorentzian functions and Shirley background.

2.5. Microindentation and Ring Compression test

A Bruker micro-hardness tester (TUKON-1202) was used to perform hardness measurements following ASTM standards [79]. Hardness testing was performed with 100 gf applied load (0.98 N of applied force) and 15 s dwell time. For hardness measurements, tube specimens were mounted in epoxy and polished. Thirty measurements were taken from the cross-section of the tube specimens. Ring compression tests were carried out to assess the mechanical properties of FeCrAl alloys pre- and post-CHF testing. An MTS Insight 30, with 30 kN load capacity, was used to perform the tests. Rings ~5 mm long were cut from the tubes at the region of interest and tested at a 1 mm/min loading rate. Due to instrument limitations, the samples were not tested until their failure but were compressed up to 6 mm.

2.6. Materials characterization

A FIB-SEM (Zeiss Auriga, 30 kV) was used to mill cross-sections and investigate the oxide formation on the sample surfaces after flow boiling testing. The oxide layer thickness was measured using ImageJ (IJ 1.46r). XRD studies were performed with a Malvern empyrean instrument with a Copper target (current 40 mA, voltage 45 kV, and $\lambda_{K\alpha 1}$=1.5406 Å). During measurement, a 3 axes Chi-Phi-z stage was used to mount the samples and then patterns were collected at a 3º/min scan rate and step size of 0.013º. A SEM Phenom ProX at an operating voltage of 15 kV was used for the grain-size analysis before and after CHF testing. Before imaging, samples were immersed for 2 minutes into an etching solution, prepared by mixing 20 mL DI water (18.47 M), 30 mL hydrochloric acid (16.46 M), and 10 mL nitric acid (3.74 M). The samples were then rinsed by distilled water. The grain-size measurements were carried out using the image processing software package, ImageJ (IJ 1.46r).

3. Results and Discussion

3.1. CHF results

The flow boiling tests for FeCrAl alloy samples, APMT and C26M, were performed to record CHF events. The CHF of APMT and C26M samples were 2.54 MW/m^2 and 2.26 MW/m^2, respectively. The CHF values obtained from these experiments are comparable with other experimental results reported in the literature [65][70]. Additionally, both APMT and C26M reached to same temperature of ~ 212 ºC during CHF event. The duration of the CHF event was 0.9 s for APMT and 1.24 s for C26M. During CHF, the surface temperature abruptly increases to sufficiently high temperatures that promote surface oxidation. Tested FeCrAl samples after the flow boiling test are shown in Fig. 3.

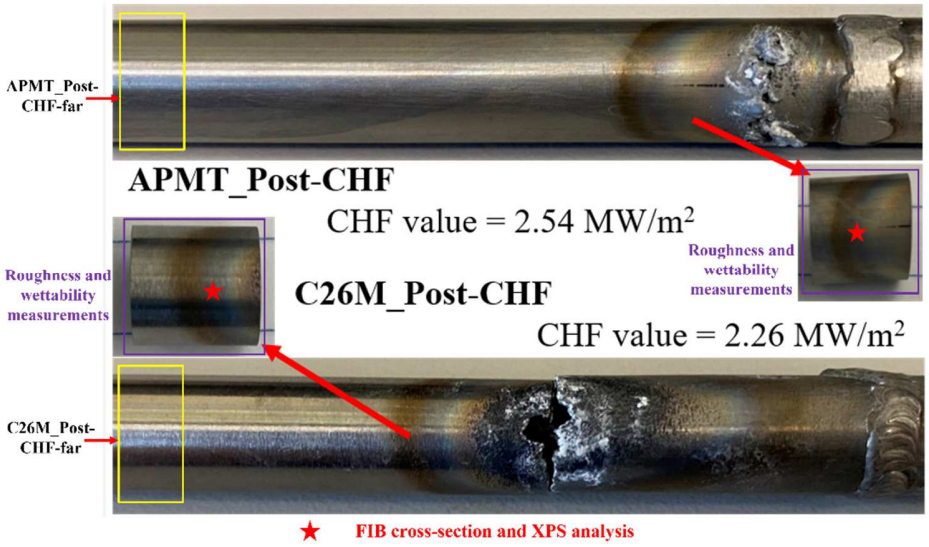

Fig. 3. FeCrAl samples after CHF testing with their CHF results.

3.2. Examination of specimens cross-sections

Fig. 4 displays SEM images of FIB-prepared cross-section for APMT_Post-CHF (Fig. 4(a)) and C26M_Post-CHF (Fig. 4(b)). To protect the oxide layer during the milling process in FIB, a thin Pt layer was deposited on the sample surfaces. These micrographs evidenced the formation of an oxide layer after flow boiling testing for both FeCrAl alloys. The oxide layer, indicated by red arrows, was ~90 nm thick for APMT_Post-CHF, while a thicker layer of ~173 nm was observed for the C26M_Post-CHF. The significant difference in the oxide layer thickness could be attributed to the duration of the CHF event.

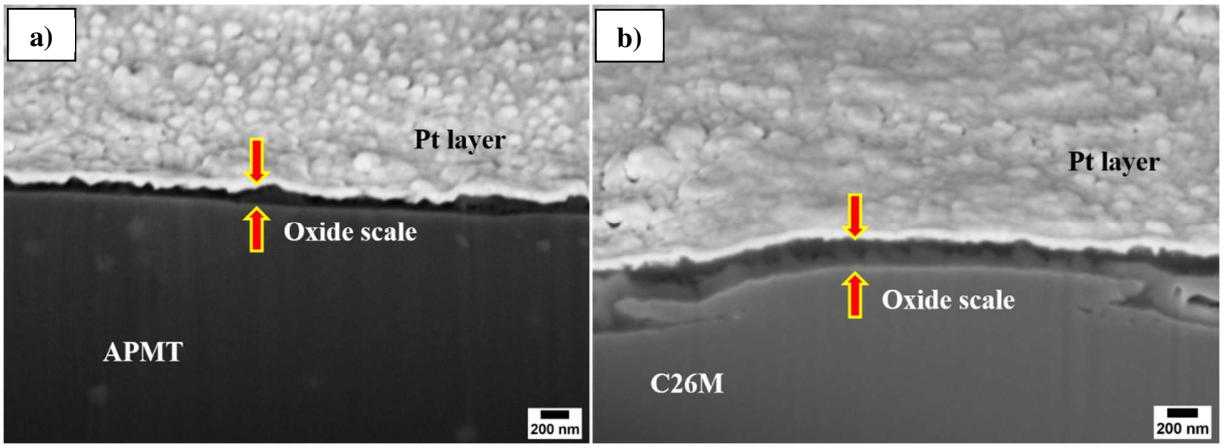

Fig. 4. Cross-sectional SEM images of FeCrAl samples after CHF testing: a) APMT_Post-CHF and b) C26M_Post-CHF (cross-sections were milled near blue region on sample surface showed in Fig. 3 (marked with red stars)).

3.3. Surface roughness

Table 4 provides three distinct surface roughness parameters measured by contact profilometry and AFM for both FeCrAl alloys before and after CHF testing. The surface roughness parameter Ra for APMT_Pre-CHF (0.4 μm) is very similar to that of commercial cladding Zircaloy-2 and Zircaloy-4 [34][35][77]. In contrast, Ra of C26M was twice that of APMT_Pre-CHF. Furthermore, the surface of the C26M_Pre-CHF, compared to that of APMT_Pre-CHF, had a higher Rz value, accompanied by a larger RSm, indicating a high average distance between two profile elements. Both FeCrAl samples evidenced a slight increase in the surface parameters after CHF testing. This result may be attributed to the oxide formation on the tubes' surface during the flow boiling testing [72].

Table 4. Roughness measurements for both types of FeCrAl surfaces before and after CHF testing.

Sample	Contact profilometry measurements (μm)			AFM measurements (nm)	
	Ra	Rz	RSm	Ra	r
APMT_Pre-CHF	0.40±0.09	3.89±0.99	70.11±7.24	205	1.02
APMT_Post-CHF	0.47±0.08	4.68±1.03	76.86±8.22	243	1.03
C26M_Pre-CHF	0.80±0.12	8.75±1.65	130.27±22.73	454	1.02
C26M_Post-CHF	0.90±0.10	9.62±1.83	138.86±22.92	550	1.04

AFM scans for the FeCrAl samples before and after CHF testing are shown in Fig. 5(a-d). The results confirmed a rougher nanoscale surface profile of the C26M_Pre-CHF sample compared to the APMT_Pre-CHF. Similarly, post-CHF samples evidenced an increased surface roughness compared to

their corresponding pre-CHF samples, supporting the results found in contact profilometry. However, the lower values of the measured surface parameters by AFM can be attributed to a different length scale of both techniques. For example, the Ra values give similar trends to those seen in contact profilometry, but their magnitudes are different. The roughness parameter Ra and roughness factor r, measured by AFM, were recorded for three scans from each sample, and the average values are presented in Table 4. By definition, the roughness factor r is the ratio of the actual measured area to the projected area [80]. The measurements showed a Ra of 205 nm for APMT_Pre-CHF, while it was 454 nm for C26M_Pre-CHF. Insignificant changes in roughness values were recorded after CHF testing. The AFM roughness data help understand the surface morphology at the nanoscale and valid the surface roughness measured using stylus profilometry.

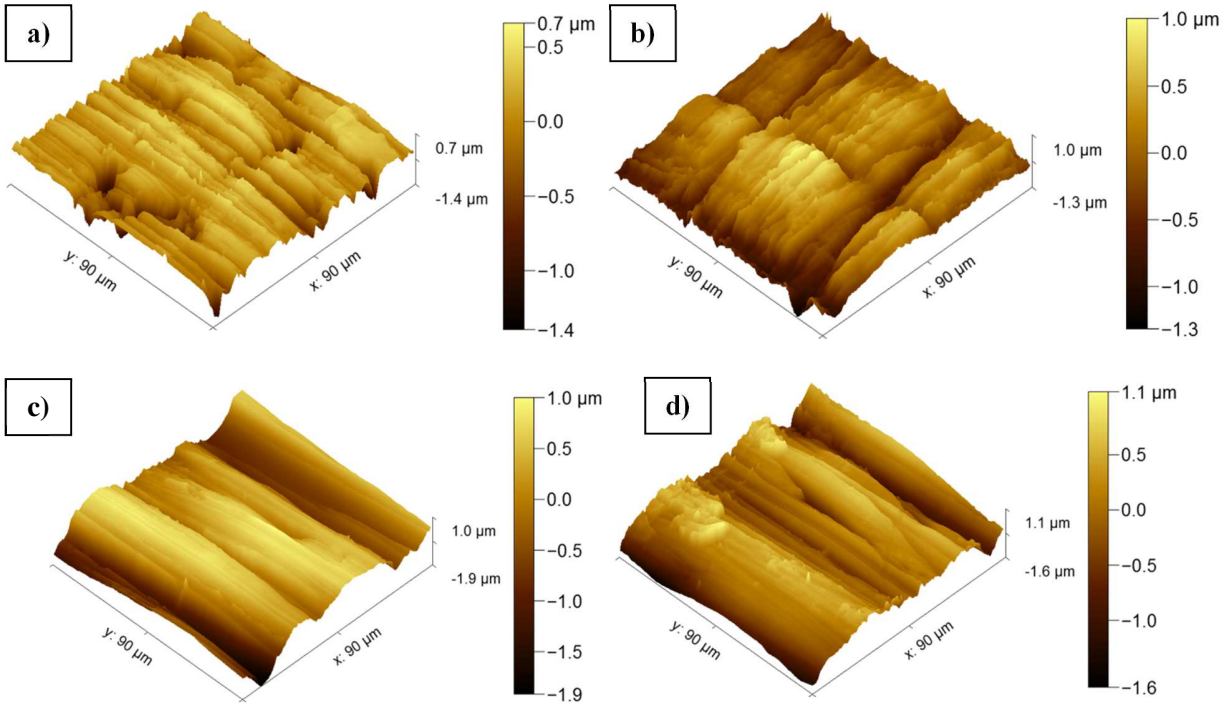

Fig. 5. Surface topography by AFM: a) APMT_Pre-CHF, b) APMT_Post-CHF, c) C26M_Pre-CHF and d) C26M_Post-CHF (Here, a and b & c and d do not correspond to the same region on the sample surface).

3.4. Wettability

In surface science, the contact angle is commonly used to characterize surface wettability. When the static water contact angle θ is < 90º, surface is identified as hydrophilic and hydrophobic when θ is > 90º [81]. A comparison of the average static contact angle for both FeCrAl types is shown in Fig. 6(a). The

C26M demonstrated a lower contact angle than the APMT sample before the CHF testing (Fig. 6(a)). For hydrophilic surfaces, the influence of surface roughness on wetting and the spreading phenomena has been evidenced in the literature [82][83]. For instance, the Zircaloy sample showed 28% decrease in contact angle when surface roughness changed from 0.52 μm to 0.58 μm [84]. Many studies have reported correlations between surface roughness and contact angle for different materials and concluded that the big scratches on the surface improve capillary wicking, which causes additional movement of the triple contact line [85][86]. This behavior was also observed in our results, where the increase in surface roughness after CHF testing led to an increase in the material's wettability. As shown in Fig. 6(a), a lower contact angle was logged for both FeCrAl alloys post-CHF.

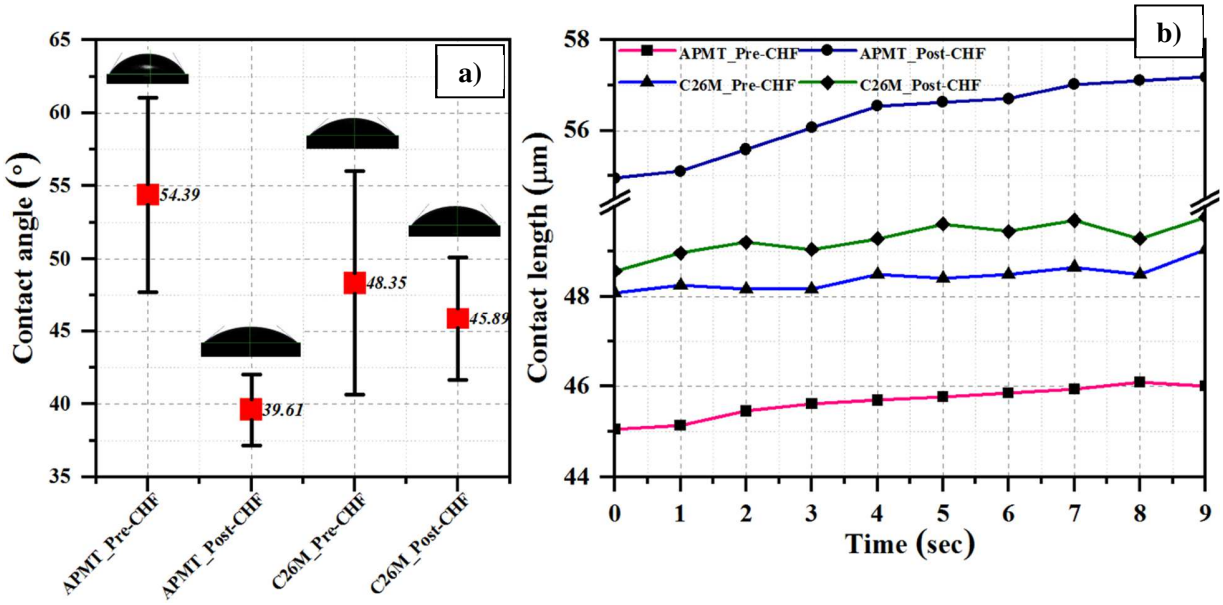

Fig. 6. Wetting characteristics of FeCrAl alloys: a) Static contact angle measured for the set of samples, and b) Droplet spreading for FeCrAl alloys before and after CHF test.

For hydrophilic and superhydrophilic surfaces, when the droplet is deposited on the surface, liquid absorption and rapid angle transition occur, also known as liquid spreading [82]. Thus, the static contact angle measurements are not enough to distinguish the wetting characteristics of these surfaces. As such, the dynamic wetting behavior of FeCrAl surfaces before and after CHF testing was characterized following the development of the water droplet with dynamic droplet-imaging experiments. Fig. 6(b) shows the spreading of a water droplet (5 μL DI) measured by contact length within 10 seconds for all FeCrAl samples. According to these results, a water droplet spreads faster on the C26M_Pre-CHF than APMT_Pre-CHF, which can be realized by the materials' higher roughness values and higher wettability. However, the spreading of APMT_Post-CHF was high among all tested samples.

3.5. XPS compositional analysis and oxidation behavior

The FeCrAl surfaces after CHF testing were investigated with XPS to understand the materials' surface chemistry. The samples were sputtered at selected time (2 min) intervals to obtain the compositional depth profiles, 150 cycles for APMT_Post-CHF (total sputtering time of 300 min) and 200 cycles for C26M_Post-CHF (total sputtering time of 400 min). The sputtering rate (nm/min) was difficult to quantify due to the presence of different species in the oxide layer and the shallow depth at the end of sputtering. However, the authors are aware that the relative sputter rate depends on the material nature. For example based on the literature, sputtering rate under certain ion beam conditions can be classified as: $C > SiC > SiO_2 > Fe_3O_4 > Cr_2O_3$ [87][88][89][90][91]. The compositional depth profile results of APMT_Post-CHF and C26M_Post-CHF are shown in Fig. 7(a-b). The high oxygen concentration in the APMT_Post-CHF sample (Fig. 7(a)) was evident up to about 80 min of sputtering, while it was observed up to 250 min of sputtering for the C26M_Post-CHF sample (Fig. 7(b)). These results are comparable with the oxide layer thickness estimated from cross-sectional SEM images in Fig. 4(a-b). In these results for both samples, a thin Si-rich layer was identified. It was unclear whether the thin Si-rich layer was from the flow boiling facility during testing or from the material itself. During depth profiling, the high-resolution XPS spectra of Al2p, Fe2p, and Cr2p were collected at different depths and deconvoluted to elucidate their chemical state. Deconvoluted spectra for both APMT_Post-CHF and C26M_Post-CHF are shown in Fig. 8 and Fig. 9, respectively. Additionally, high-resolution spectra for pre-CHF samples, APMT_Pre-CHF and C26M_Pre-CHF, were collected to serve as a reference (Fig. 10). In all high-resolution spectra, original spectra collected from XPS are represented with black dotted lines; however, the thin brown line is the fitted profile. The positions in binding energy and intensities of the peaks associated with each element allowed the identification of their oxidation states [92][93][94][95][96][97]. The multi-peak fitting was adopted to analyze all XPS patterns [96].

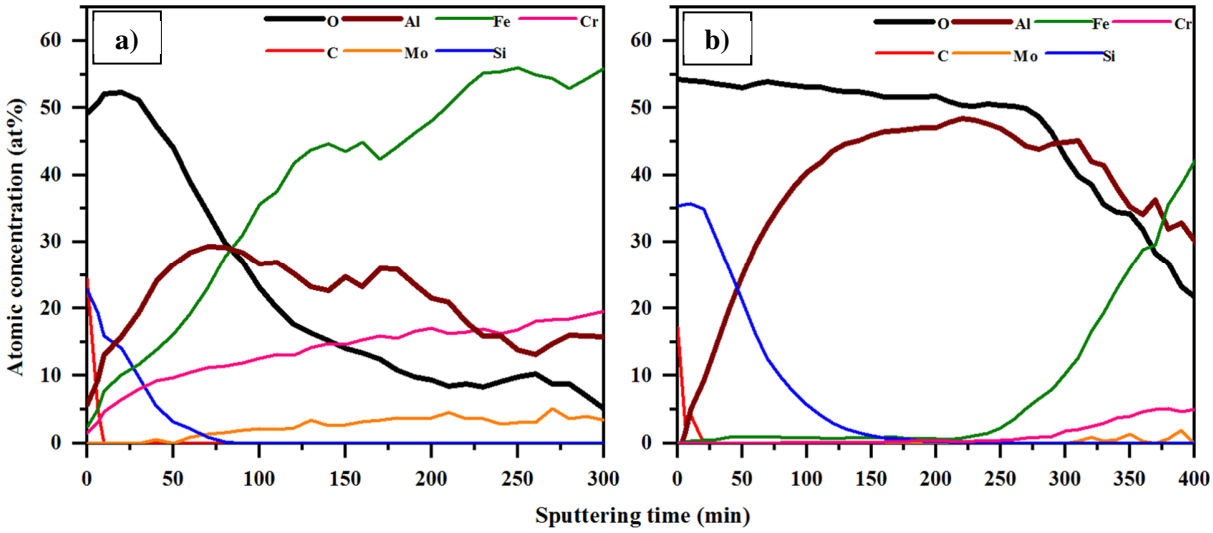

Fig. 7. Element composition vs. depth (sputter time) profile on the post-CHF samples surface (marked with red stars in Fig. 3): a) APMT_Post-CHF and b) C26M_Post-CHF sputtering using Ar+ ion with 3 keV beam energy.

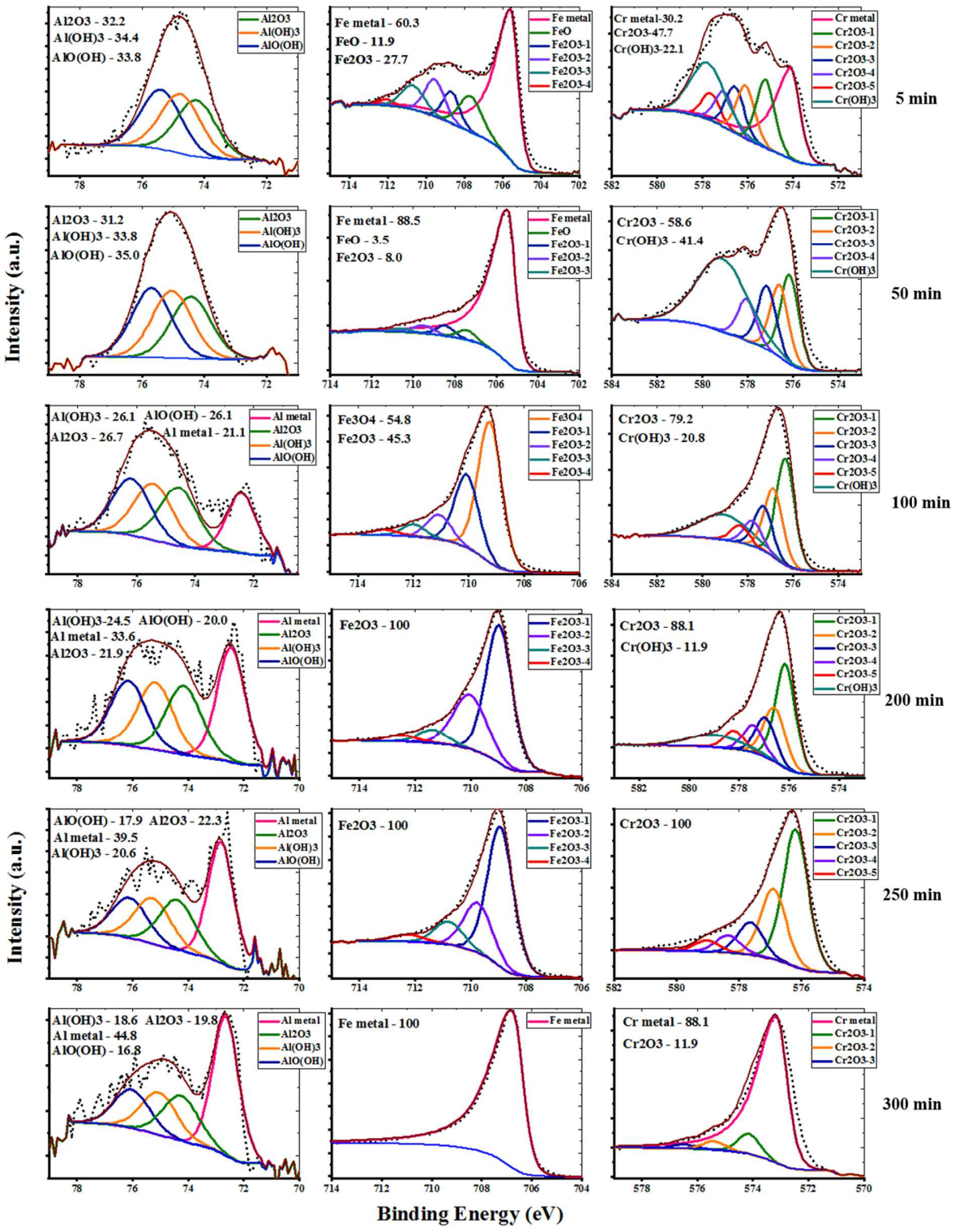

Fig. 8. XPS high-resolution spectra for Al2p, Fe2p and Cr2p at various depths for the APMT_Post-CHF sample (each present species was calculated in % area).

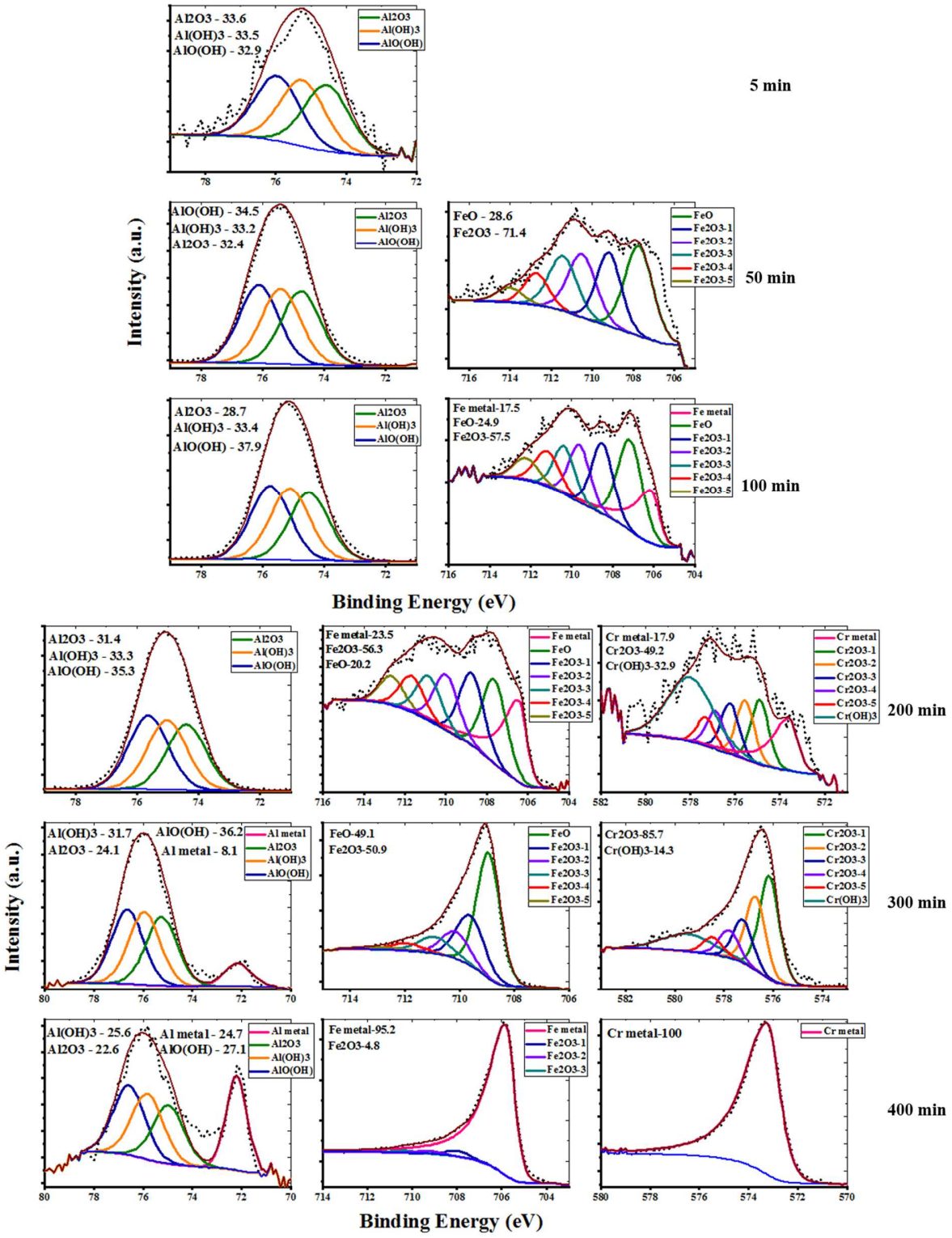

Fig. 9. XPS high-resolution spectra for Al2p, Fe2p and Cr2p at various depths for the C26M_Post-CHF sample (each present species was calculated in % area).

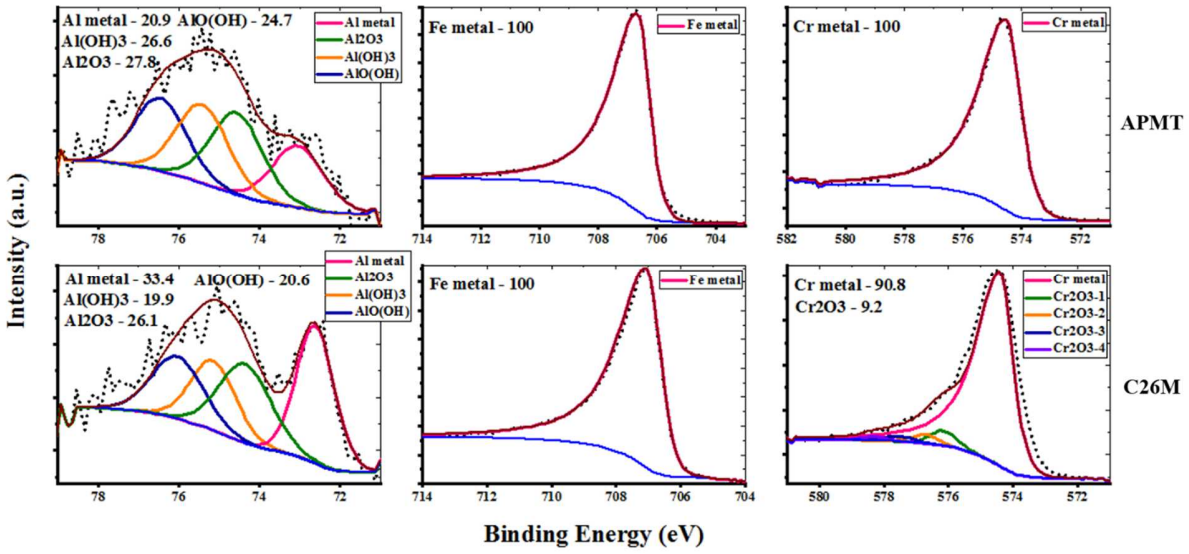

Fig. 10. XPS high-resolution spectra for Al2p, Fe2p and Cr2p for the APMT_Pre-CHF and C26M_Pre-CHF samples (each present species was calculated in % area).

The diagrams in Fig. 11 give a qualitative representation of the contribution from the different oxide species on the FeCrAl samples, APMT_Post-CHF (a) and C26M_Post-CHF (b), tested in the CHF facility. These graphs were based on the high-resolution XPS spectra collected during depth profiling, where X-axis reads sputtering times at which high-resolution spectra were collected. When samples were tested in the flow boiling system, working fluid (DI water) reacts with the sample surface by means of oxidation and adsorption, producing Al_2O_3, $Al(OH)_3$, AlO(OH), FeO, Fe_2O_3, Fe_3O_4, Cr_2O_3, and $Cr(OH)_3$. Alloying elements, Fe, Cr, and Al, would react with O based on their distribution on the surface. For the APMT_Post-CHF sample, the mixed oxide film in the first stage of sputtering (5 min in Fig. 11(a)) was mainly composed of Al oxides and hydroxides with a noticeable amount of Fe, Cr, and their corresponding oxides and hydroxides. In contrast, in the C26M_Post-CHF sample, the layer was detected with only aluminum oxides and hydroxides (Fig. 11(b)). It was assumed that O^{2-} stops reacting with alloy elements on the surface once a thin film of pure/mixed oxide formed on the surface. However, because of the existence of mixed oxide film, internal diffusion of O^{2-} was enough to produce more Al_2O_3, $Al(OH)_3$, AlO(OH), Fe_2O_3, Fe_3O_4, and Cr_2O_3. Thus, the oxidation process results from adsorption, ionization, and diffusion of oxidizing species. In the sputtering time between 5 to 100 min, the presence of Al_2O_3, $Al(OH)_3$, and AlO(OH) was predominant for both post CHF samples. The possible reaction of Al with water leads to the products identified in this work, which are thermodynamically favorable from room temperature to temperatures even above the aluminum melting point of 660 ºC [98]. The aluminum hydroxides are the precursors of alumina, and their thermodynamical stability as a function of

temperature has indicated that the higher the temperature, the lower the degree of hydration [98]. The phase stability diagrams indicate three different domains i) $Al(OH)_3$ is the most stable product from room temperature to 280 ºC, ii) AlO(OH) is the most stable in the temperature range from 280 to 480 ºC and iii) Al_2O_3 is the most stable product above 480 ºC. According to the stability diagrams, our results indicate that the analyzed region in the material reached a temperature high enough to promote the formation of alumina. However, this phase did not fully develop as the test was stopped when the CHF was reached. Thus, the fraction of the different products in the material surface is $AlO(OH)>Al(OH)_3>Al_2O_3$. The C26M_Post-CHF samples also showed FeO and Fe_2O_3, along with the aluminum oxides/hydroxides, with no evidence of Cr oxides. For the APMT_Post-CHF sample, at depths given by the sputtering times from 100 min to 250 min, the formation of Fe_2O_3 was favored. A similar effect was seen for the C26M_Post-CHF sample during sputtering times between 200 to 300 min. For both samples, at the highest sputtering time used in this experiment, when the concentration of O^{2-} at the interface (mixed oxide film/matrix) was too low to promote oxide formation, it led to negligible amounts of Al and Cr oxides in APMT_Post-CHF sample and some Al and Fe oxides in C26M_Post-CHF sample. At this point, the area percentage of all elements and their species at different valence states are almost similar to the results of deconvoluted high-resolution spectra of pre-CHF FeCrAl samples, shown in Fig. 10.

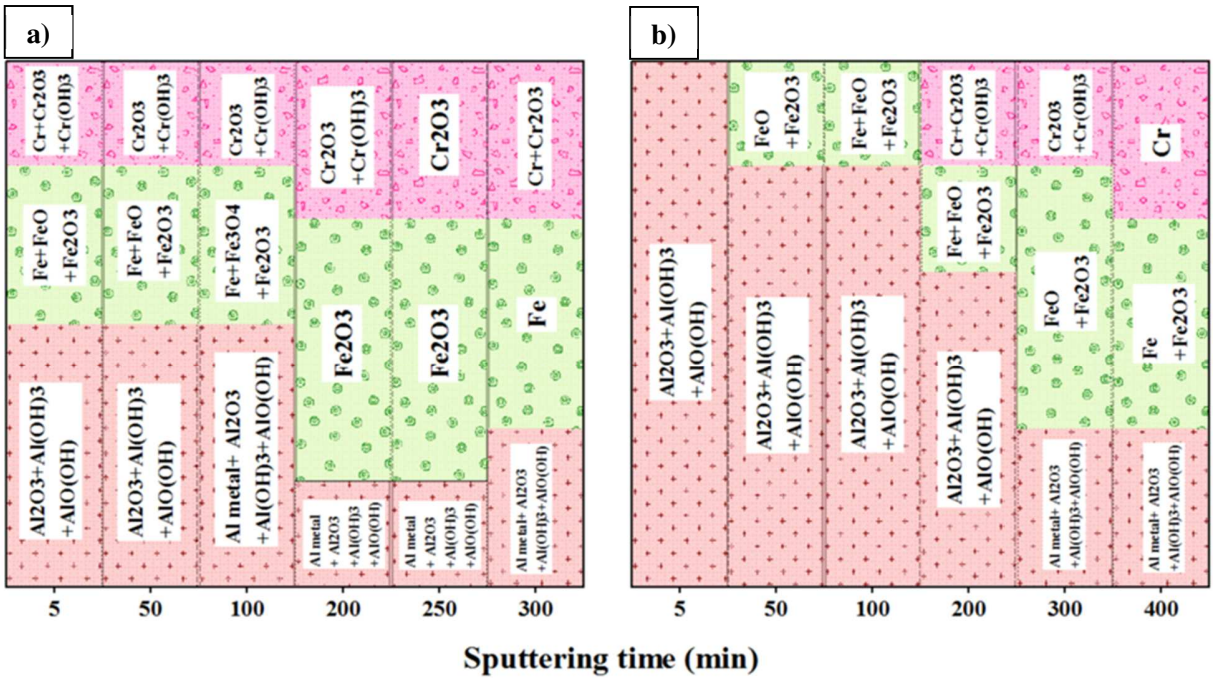

Fig. 11. Oxidation behavior diagram of FeCrAl after CHF testing: a) APMT_Post-CHF and b) C26M_Post-CHF.

The surface characterization and surface chemistry analysis data presented in this section demonstrated the evolution of FeCrAl surface when tested into flow boiling CHF testing. Our results discussed above indicate that CHF tested samples evidence improved wettability of the sample, possibly the consequence of the presence of various oxide and hydroxides species. After flow boiling CHF testing, FeCrAl alloy surface chemistry changes can be considered responsible for increasing surface wettability. In contrast, in our previous studies, the post-CHF Cr-coated (PVD coating) samples showed poor wettability because of the adsorption of contaminants [34][35]. However, in this study, a negligible amount of surface contaminations was recorded for FeCrAl samples after CHF testing, contributing to the hydrophilic characteristics of the exposed samples. Effects of surface contaminants on wetting characteristics are reported in the literature [99].

3.6. Ring compression test and Hardness measurements

The ring compression test data for all FeCrAl samples is shown in Fig. 12(a). An inset picture of the sample tubes before and after compression is also added here with load dies. The engineering stress-strain curves (Fig. 12(a) followed a similar trend for both types of FeCrAl alloys before and after CHF testing. Before CHF testing, the APMT_Pre-CHF sample evidenced higher yield strength (the yield strength values were calculated at 0.2% strains) and peak load than C26M_Pre-CHF (Table 5) which agrees with results in the literature for FeCrAl alloys with different Al and Cr content [100]. The overall strength of both APMT_Post-CHF and C26M_Post-CHF was found to be higher than the Pre-CHF testing samples. Additionally, peak loads for APMT_Post-CHF-far and C26M_Post-CHF-far were slightly lower (Table 5) compared to those obtained from CHF regions of corresponding samples. The difference could be because of axial thermal gradients during the testing of the tubes. Fig. 12(b) shows the comparison of hardness measurements before and after CHF testing for both types of FeCrAl alloy taken with 0.98 N load. The hardness of APMT was almost 30 % higher than the C26M sample, which may be attributed to the higher Cr content in APMT compared to C26M [100][101]. After CHF testing, the hardness of both FeCrAl alloys slightly increased. The hardness obtained from the yellow region in Fig. 3 were 3.41 GPa and 2.80 GPa for APMT_Post-CHF-far and C26M_Post-CHF-far, respectively. These values are slightly lower compared to values obtained from the purple region in Fig. 3. The hardness values of FeCrAl alloys obtained herein are comparable with previous reports [50][102].

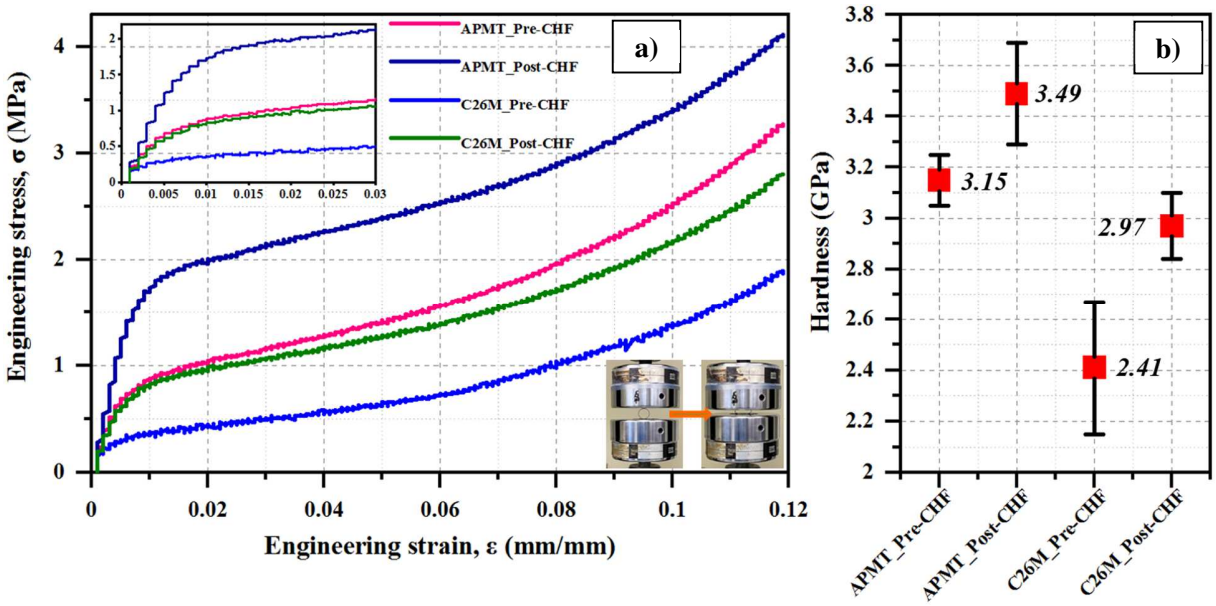

Fig. 12. Comparison of mechanical properties of FeCrAl alloys before and after CHF testing: a) Ring compression tests and b) Microindentation tests.

Table 5. Ring compression test results before and after CHF testing.

Sample	Parameter	
	Peak load (N)	Yield strength (Mpa)
APMT-Pre_CHF	156	0.90
APMT-Post_CHF	188	1.76
APMT-Post_CHF-far	171	-
C26M-Pre_CHF	97	0.38
C26M-Post_CHF	153	0.83
C26M-Post_CHF-far	130	-

3.7. Microstructure of the FeCrAl alloys

The XRD patterns of the FeCrAl alloys before and after CHF testing are presented in Fig. 13(a). The diffraction peaks for all samples were observed at 2θ° of 44.27°, 64.38°, and 81.40° confirmed the body-centered cubic (BCC) crystal structure (ICDD pdf #00-054-0387) [77]. Due to the lower atomic packing factor, BCC structures exhibit smaller volume expansion associated with the insertion of an interstitial atom, hence offering higher dimensional stability during neutron irradiation [50][103]. The peaks in the XRD pattern of the C26M-Pre_CHF sample compared to those in APMT-Pre_CHF showed up at slightly lower angles, which may be due to the higher Al content (Fig. 13(a)). The Bragg equation, $2d\sin\theta=n\lambda$

(where d, lattice parameter; θ, diffraction angle; n, diffraction series; and λ, beam wavelength) shows the relationship between how the diffraction angle decreases by increasing the lattice parameter when the diffraction series and beam wavelength are fixed [104]. The lattice parameter increases with the Al content because of the larger atomic radius of Al compared to Fe [105]. Furthermore, a close inspection of the XRD peak profiles indicated a variation of the FWHM for post-CHF specimens. The calculated FWHM, using Voigt curve fitting [106], for the (110) peak for both post-CHF FeCrAl samples are shown in Fig. 13(b). The results indicate a significant decrease in FWHM of the peaks for both FeCrAl samples after CHF testing, which can be attributed to a reduction in dislocation density and residual stresses. This observation correlates with the mechanical properties of the materials post-CHF [107]. The slight shifting of (110) peak for the post-CHF FeCrAl has been attributed to minor displacements of the sample from the center of the XRD goniometer due to their curved geometry [108].

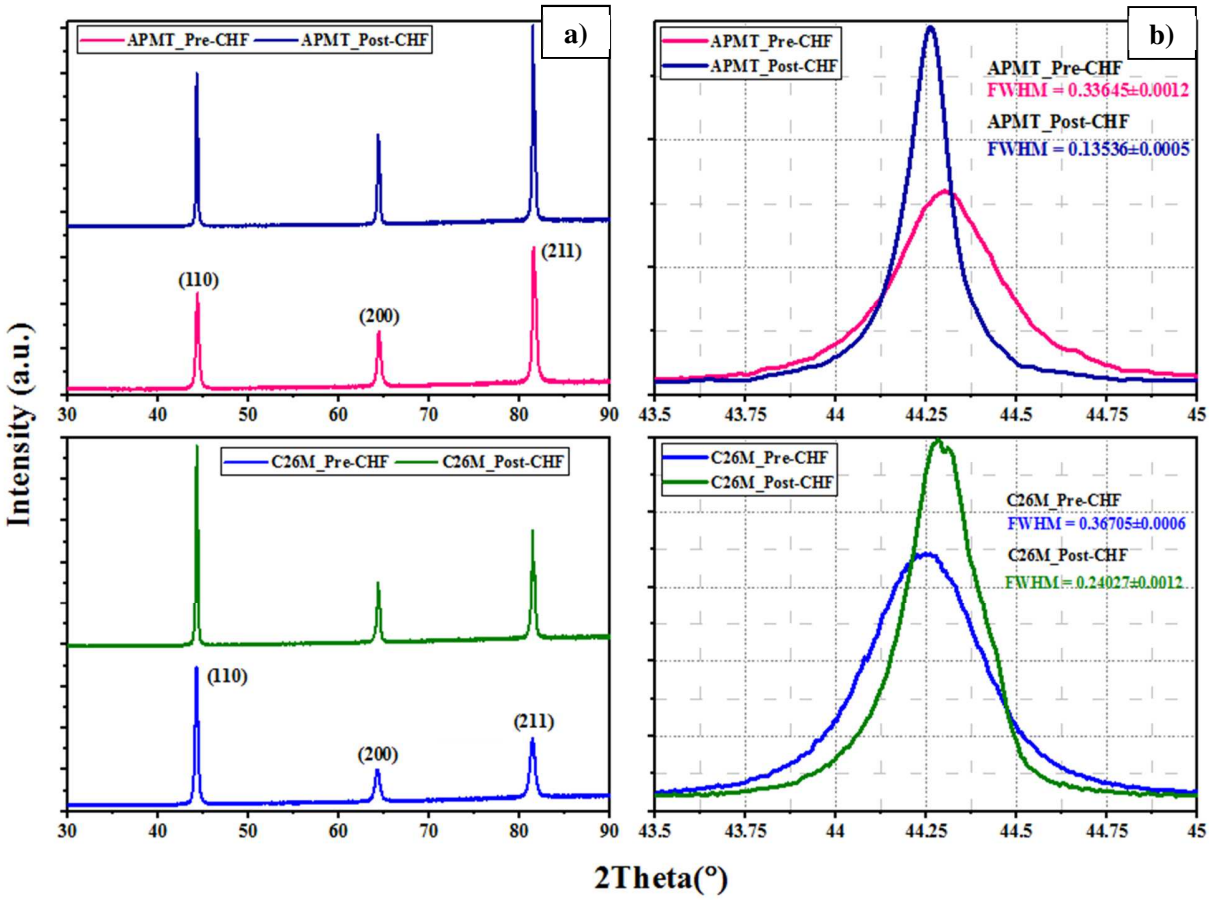

Fig. 13. X-ray diffraction pattern of the FeCrAl alloys before and after CHF testing (a) and showing effect of CHF testing on peak broadening (b).

The grain size of all FeCrAl samples, APMT_Pre-CHF, C26M_Pre-CHF, APMT_Post-CHF, and C26M_Post-CHF, was determined using the SEM cross-sections. Fig. 14(a-b) shows the micrographs of the APMT_Pre-CHF and C26M_Pre-CHF previously etched to reveal grain boundaries. The measured average grain-size of the samples before CHF testing was 7.78±3.38 μm for APMT_Pre-CHF and 46.92±15.42 μm for C26M_Pre-CHF. The significant difference in grain size and microstructure is associated to the different fabrication methods: traditional melting and forging for the C26M and powder metallurgy process for APMT [50]. Newer versions of C26M cladding are being fabricated using powder metallurgy technology, which renders smaller grain sizes than the traditional melting method. Additionally, due to the larger atomic radius of Al compared to Fe, the lattice constant of ferrite increases with the Al content, which enhances atomic diffusion and promotes grain growth during solidification [105]. With comparatively smaller grain size, the APMT has evidenced higher overall strength in this study, which agrees with previous studies in the literature [109]. The measured average grain-size of APMT_Post-CHF was 7.0±3.3 μm, while it was 44.2±15.3 μm for C26M_Post-CHF. These results did not show significant changes in the grain-size for the post-CHF samples.

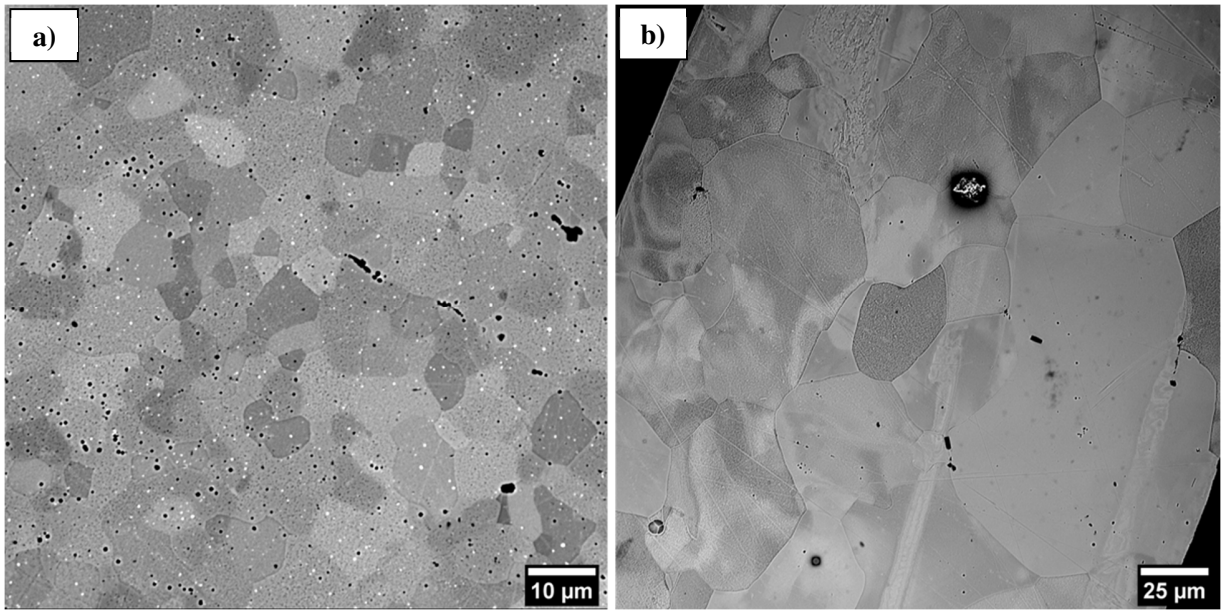

Figure 14. SEM micrographs of etched samples: a) APMT_Pre-CHF and b) C26M_Pre-CHF.

The implementation of FeCrAl alloys as accident tolerant fuels in LWR relies on their high resistance to degradation at high temperatures and their better performance compared to standard materials under normal operating conditions. During the flow boiling CHF experiments performed herein, the FeCrAl alloys evidenced their ability to rapidly react to the temperature rise during the CHF event forming oxides

on the surface, which also led to an improved surface wettability and roughness. These surface properties of both FeCrAl alloys may result in the enhanced thermal-hydraulic performance of the materials compared to the current bare Zircaloy cladding tubes.

4. Summary and Conclusions

Cladding tubes of FeCrAl alloys APMT and C26M were tested in a flow boiling testing facility at atmospheric pressure. The surface characteristics, mechanical properties, and microstructural features of the FeCrAl alloys were studied before and after CHF testing through XPS, contact profilometry, AFM, contact angle goniometry, microindentation and ring compression, FIB-SEM, and XRD. After the flow boiling test, the formation of an oxide layer was evidenced in the cross-sectional examination of both alloys. Analysis of the two materials' topography showed higher roughness parameters, which may result from the surface oxide formation during CHF transient testing. The detailed early-stage oxidation of the alloys was studied using XPS depth profiling with the high-resolution spectra of Al2p, Fe2p, and Cr2p elements. The results revealed a thin layer of aluminum oxides and hydroxides mixed, with a small fraction of other elements and their oxides for APMT_Post-CHF. A pure Al_2O_3/ $Al(OH)_3$/ AlO(OH) layer was detected for the C26M_Post-CHF sample. Similarly, the increase in the materials' wettability has been attributed to the hydrophilic behavior of the aluminum species formed on the materials' surface. Hardness was slightly increased for both FeCrAl samples after CHF testing. However, compared to C26M, the APMT sample showed almost 30% higher hardness before and 15% higher after flow boiling testing. The increase of peak load and yield strength was recorded for both types of FeCrAl alloys due to CHF testing. Higher overall mechanical properties of APMT over C26M may be attributed to their different grain size. XRD patterns revealed the sharpening of the peaks after flow boiling testing, indicating lower dislocation density. The post-CHF transient higher hardness is not expected to affect the performance of the two materials in their cladding function.

5. Acknowledgments

This research was funded by the U.S. Department of Energy's office of Nuclear Energy under the Nuclear Engineering University Program (Project number: 17-13-019). The authors would like to thank the Department of Mechanical and Nuclear Engineering at Virginia Commonwealth University (VCU) and the Mechanical Engineering Department University at the Wisconsin-Madison for their support. The authors also want to thank the staff at the Nanomaterials Core Characterization Facility at VCU College of Engineering for their technical support with advanced materials characterization.

6. References

[1] S.J. Zinkle, K.A. Terrani, J.C. Gehin, L.J. Ott, L.L. Snead, Accident tolerant fuels for LWRs: A

perspective, J. Nucl. Mater. 448 (2014) 374–379. https://doi.org/10.1016/j.jnucmat.2013.12.005.

[2] K.A. Terrani, Accident tolerant fuel cladding development: Promise, status, and challenges, J. Nucl. Mater. 501 (2018) 13–30. https://doi.org/10.1016/j.jnucmat.2017.12.043.

[3] T. Cheng, J.R. Keiser, M.P. Brady, K.A. Terrani, B.A. Pint, Oxidation of fuel cladding candidate materials in steam environments at high temperature and pressure, J. Nucl. Mater. 427 (2012) 396–400. https://doi.org/10.1016/j.jnucmat.2012.05.007.

[4] R.B. Rebak, Alloy Selection for Accident Tolerant Fuel Cladding in Commercial Light Water Reactors, Metall. Mater. Trans. E. 2 (2015) 197–207. https://doi.org/10.1007/s40553-015-0057-6.

[5] B.A. Pint, K.A. Terrani, Y. Yamamoto, L.L. Snead, Material Selection for Accident Tolerant Fuel Cladding, Metall. Mater. Trans. E. 2 (2015) 190–196. https://doi.org/10.1007/s40553-015-0056-7.

[6] Y.-H. Koo, J.-H. Yang, J.-Y. Park, K.-S. Kim, H.-G. Kim, D.-J. Kim, Y.-I. Jung, K.-W. Song, KAERI's Development of LWR Accident-Tolerant Fuel, Nucl. Technol. 186 (2014) 295–304. https://doi.org/10.13182/nt13-89.

[7] J.C. Brachet, M. Le Saux, T. Guilbert, M. Tupin, On-going studies at CEA on chromium coated zirconium based nuclear fuel claddings for enhanced Accident Tolerant LWRs Fuel, TopFuel 2015, (13-19 Sept. 2015), Zurich, Switzerland.

[8] H.G. Kim, J.H. Yang, W.J. Kim, Y.H. Koo, Development Status of Accident-tolerant Fuel for Light Water Reactors in Korea, Nucl. Eng. Technol. 48 (2016) 1–15. https://doi.org/10.1016/j.net.2015.11.011.

[9] B. Cheng, Y.J. Kim, P. Chou, Improving Accident Tolerance of Nuclear Fuel with Coated Mo-alloy Cladding, Nucl. Eng. Technol. 48 (2016) 16–25. https://doi.org/10.1016/j.net.2015.12.003.

[10] K.G. Field, X. Hu, K.C. Littrell, Y. Yamamoto, L.L. Snead, Radiation tolerance of neutron-irradiated model Fe-Cr-Al alloys, J. Nucl. Mater. 465 (2015) 746–755. https://doi.org/10.1016/j.jnucmat.2015.06.023.

[11] K. Shimoda, T. Hinoki, H. Kishimoto, A. Kohyama, Enchanced high-temperature performances of SiC/SiC composites by high densification and crystalline structure, Compos. Sci. Technol. 71 (2011) 326–332. https://doi.org/10.1016/j.compscitech.2010.11.026.

[12] C.P. Deck, G.M. Jacobsen, J. Sheeder, O. Gutierrez, J. Zhang, J. Stone, H.E. Khalifa, C.A. Back, Characterization of SiC-SiC composites for accident tolerant fuel cladding, J. Nucl. Mater. 466 (2015) 1–15. https://doi.org/10.1016/j.jnucmat.2015.08.020.

[13] R.B. Rebak, Accident Tolerant Materials for Light Water Reactor Fuels, Elsevier, 2020. https://books.google.com/books?id=hSzJDwAAQBAJ.

[14] K. Barrett, S. Bragg-Sitton, D. Galicki, Advanced LWR Nuclear Fuel Cladding System Development Trade-off Study, Idaho 83415 INL/EXT-12-27090. (2012) 1–34.

https://doi.org/10.2172/1057698.

[15] C. Tang, M. Stueber, H.J. Seifert, M. Steinbrueck, Protective coatings on zirconium-based alloys as accident-Tolerant fuel (ATF) claddings, Corros. Rev. 35 (2017) 141–165. https://doi.org/10.1515/corrrev-2017-0010.

[16] B. Maier, H. Yeom, G. Johnson, T. Dabney, J. Walters, J. Romero, H. Shah, P. Xu, K. Sridharan, Development of Cold Spray Coatings for Accident-Tolerant Fuel Cladding in Light Water Reactors, Jom. 70 (2018) 198–202. https://doi.org/10.1007/s11837-017-2643-9.

[17] Y. Ren, S. Zou, M. Lei, W. Xiao, X. Zhou, D. Tang, H. Deng, C. Xiao, Y. Chen, Effect of roughness of substrate and sputtering power on the properties of TiN coatings deposited by magnetron sputtering for ATF, J. Nucl. Mater. 509 (2018) 542–549. https://doi.org/10.1016/j.jnucmat.2018.07.011.

[18] H.G. Kim, I.H. Kim, Y.I. Jung, D.J. Park, J.H. Yang, Y.H. Koo, Development of Surface Modified Zr Cladding by Coating Technology for ATF, Top Fuel 2016. (2016) 1157–1163.

[19] V.N. Voyevodin, A.S. Kuprin, E.N. Reshetnyak, V.D. Ovcharenko, R.L. Vasilenko, V.V. Bryk, V.A. Belous, P.N. V'yugov, G.N. Tolmachova, Vacuum-arc chromium-based coatings for protection of zirconium alloys from the high-temperature oxidation in air, J. Nucl. Mater. 465 (2015) 400–406. https://doi.org/10.1016/j.jnucmat.2015.06.016.

[20] H.G. Kim, I.H. Kim, Y. Il Jung, D.J. Park, J.Y. Park, Y.H. Koo, Adhesion property and high-temperature oxidation behavior of Cr-coated Zircaloy-4 cladding tube prepared by 3D laser coating, J. Nucl. Mater. 465 (2015) 531–539. https://doi.org/10.1016/j.jnucmat.2015.06.030.

[21] B. Fotovvati, N. Namdari, A. Dehghanghadikolaei, On Coating Techniques for Surface Protection: A Review, J. Manuf. Mater. Process. 3 (2019) 28. https://doi.org/10.3390/jmmp3010028.

[22] Z. Yao, J. Stiglich, T.S. Sudarshan, Molybdenum silicide based materials and their properties, J. Mater. Eng. Perform. 8 (1999) 291–304. https://doi.org/10.1361/105994999770346837.

[23] D. V. Sidelev, E.B. Kashkarov, M.S. Syrtanov, V.P. Krivobokov, Nickel-chromium (Ni–Cr) coatings deposited by magnetron sputtering for accident tolerant nuclear fuel claddings, Surf. Coatings Technol. 369 (2019) 69–78. https://doi.org/10.1016/j.surfcoat.2019.04.057.

[24] J. Krejci, M. Sevecek, DEVELOPMENT OF CHROMIUM AND CHROMIUM NITRIDE COATED CLADDING 2017 Water Reactor Fuel Performance Meeting, (2017).

[25] M. Wagih, B. Spencer, J. Hales, K. Shirvan, Fuel performance of chromium-coated zirconium alloy and silicon carbide accident tolerant fuel claddings, Ann. Nucl. Energy. 120 (2018) 304–318. https://doi.org/10.1016/j.anucene.2018.06.001.

[26] R. Hui, W. Cook, C. Sun, Y. Xie, P. Yao, J. Miles, R. Olive, J. Li, W. Zheng, L. Zhang, Deposition, characterization and performance evaluation of ceramic coatings on metallic

substrates for supercritical water-cooled reactors, Surf. Coatings Technol. 205 (2011) 3512–3519. https://doi.org/10.1016/j.surfcoat.2010.12.017.

[27] A. Wu, J. Ribis, J.C. Brachet, E. Clouet, F. Leprêtre, E. Bordas, B. Arnal, HRTEM and chemical study of an ion-irradiated chromium/zircaloy-4 interface, J. Nucl. Mater. 504 (2018) 289–299. https://doi.org/10.1016/j.jnucmat.2018.01.029.

[28] H.G. Kim, Y.I. Jung, J.H. Park, D.J. Park, Y.H. Koo, J. Park, High temperature steam-oxidation behavior of arc ion plated Cr coatings for accident tolerant fuel claddings, Surf. Coatings Technol. 280 (2015) 256–259. https://doi.org/10.1016/j.surfcoat.2015.09.022.

[29] M. Shahin, J. Petrik, A. Seshadri, B. Phillips, K. Shirvan, Experimental investigation of cold-spray chromium cladding, Topfuel. (2018) 1–10.

[30] M. Ševecek, J. Krejci, M.H. Shahin, J. Petrik, R.G. Ballinger, K. Shirvan, Fatigue Behavior of Cold Spray - Coated Accident Tolerant, Topfuel. (2018) 1–15.

[31] J.C. Brachet, M. Dumerval, V. Lezaud-Chaillioux, M. Le Saux, E. Rouesne, D. Hamon, S. Urvoy, T. Guilbert, Q. Houmaire, C. Cobac, G. Nony, J. Rousselot, F. Lomello, F. Schuster, H. Palancher, J. Bischoff, E. Pouillier, Behavior of Chromium Coated M5 Claddings under LOCA Conditions, 2017 Water React. Fuel Perform. Meet. 2017 Water React. Fuel Perform. Meet. (2017) 1–11.

[32] H. Shah, J. Romero, P. Xu, B. Maier, G. Johnson, J. Walters, T. Dabney, H. Yeom, K. Sridharan, Development of Surface Coatings for Enhanced Accident Tolerant Fuel, Water React. Fuel Perform. Meet. (2017).

[33] H.O. Behavior, O.F.C. Zirconium, H. Kim, I. Kim, Y. Jung, D. Park, J. Park, Y. Koo, I. Introduction, HIGH-TEMPERATURE OXIDATION BEHAVIOR OF CR-COATED ZIRCONIUM ALLOY, (2013) 842–846.

[34] R. V. Umretiya, B. Elward, D. Lee, M. Anderson, R.B. Rebak, J. V. Rojas, Mechanical and Chemical Properties of PVD and Cold Spray Cr-coatings on Zircaloy-4, J. Nucl. Mater. 541 (2020) 152420. https://doi.org/10.1016/j.jnucmat.2020.152420.

[35] R. V Umretiya, S. Vargas, D. Galeano, R. Mohammadi, C.E. Castano, J. V Rojas, Effect of surface characteristics and environmental aging on wetting of Cr-coated Zircaloy-4 accident tolerant fuel cladding material, J. Nucl. Mater. (2020) 152163. https://doi.org/https://doi.org/10.1016/j.jnucmat.2020.152163.

[36] J.C. Brachet, C. Lorrette, A. Michaux, C. Sauder, I. Idarraga-Trujillo, M. Le Saux, M. Le Flem, F. Schuster, A. Billard, E. Monsifrot, E. Torres, F. Rebillat, J. Bischoff, A. Ambard, CEA studies on advanced nuclear fuel claddings for enhanced Accident Tolerant LWRs Fuel(LOCA and beyond LOCA conditions), Fontevraud 8 - Contribution of Materials Investigations and Operating Experience to LWRs' Safety, Performation and Reliability, France, Avignon - 2014, Sept. 15-18.

[37] I. Idarraga-Trujillo, M. Le Flem, J.C. Brachet, M. Le Saux, D. Hamon, S. Muller, V. Vandenberghe, M. Tupin, E. Papin, E. Monsifrot, A. Billard, F. Schuster, Assessment at CEA of coated nuclear fuel cladding for LWRS with increased margins in loca and beyond loca conditions, LWR Fuel Perform. Meet. Top Fuel 2013. 2 (2013) 860–867.

[38] M. Huang, Y. Li, G. Ran, Z. Yang, P. Wang, Cr-coated Zr-4 alloy prepared by electroplating and its in situ He+ irradiation behavior, J. Nucl. Mater. 538 (2020) 152240. https://doi.org/10.1016/j.jnucmat.2020.152240.

[39] A. Jain, S. Loganathan, J.D. Kanjilal, G.K. Mehta, High energy heavy ion irradiation of chromium films, Vacuum. 46 (1995) 369–371. https://doi.org/10.1016/0042-207X(94)00081-6.

[40] V. V. Bryk, V.N. Voyevodin, I.M. Neklyudov, A.N. Rakitskij, Microstructure investigation of Cr and Cr alloys irradiated with heavy ions, J. Nucl. Mater. 225 (1995) 146–153. https://doi.org/10.1016/0022-3115(95)00066-6.

[41] Y. Lee, J.I. Lee, H.C. NO, Mechanical analysis of surface-coated zircaloy cladding, Nucl. Eng. Technol. 49 (2017) 1031–1043. https://doi.org/10.1016/j.net.2017.03.012.

[42] K.G. Field, Y. Yamamoto, B.A. Pint, M.N. Gussev, K.A. Terrani, Accident tolerant fecral fuel cladding: current status towards commercialization, Miner. Met. Mater. Ser. (2019) 1381–1389. https://doi.org/10.1007/978-3-030-04639-2_91.

[43] STEAM OXIDATION, BURST AND CRITICAL HEAT FLUX TESTING OF COMMERCIAL FECRAL CLADDING B. A. Pint, L. A. Baldesberger and K. A. Kane, (2019) 311–316.

[44] B.A. Pint, K.A. Terrani, R.B. Rebak, Steam oxidation behavior of fecral cladding, Miner. Met. Mater. Ser. (2019) 1451–1460. https://doi.org/10.1007/978-3-030-04639-2_96.

[45] R.B. Rebak, Versatile Oxide Films Protect FeCrAl Alloys Under Normal Operation and Accident Conditions in Light Water Power Reactors, Jom. 70 (2018) 176–185. https://doi.org/10.1007/s11837-017-2705-z.

[46] D.J. Park, H.G. Kim, J.Y. Park, Y. Il Jung, J.H. Park, Y.H. Koo, A study of the oxidation of FeCrAl alloy in pressurized water and high-temperature steam environment, Corros. Sci. 94 (2015) 459–465. https://doi.org/10.1016/j.corsci.2015.02.027.

[47] C. Tang, A. Jianu, M. Steinbrueck, M. Grosse, A. Weisenburger, H.J. Seifert, Influence of composition and heating schedules on compatibility of FeCrAl alloys with high-temperature steam, J. Nucl. Mater. 511 (2018) 496–507. https://doi.org/10.1016/j.jnucmat.2018.09.026.

[48] K.G. Field, S.A. Briggs, K. Sridharan, R.H. Howard, Y. Yamamoto, Mechanical properties of neutron-irradiated model and commercial FeCrAl alloys, J. Nucl. Mater. 489 (2017) 118–128. https://doi.org/10.1016/j.jnucmat.2017.03.038.

[49] E. Aydogan, J.S. Weaver, S.A. Maloy, O. El-Atwani, Y.Q. Wang, N.A. Mara, Microstructure and

mechanical properties of FeCrAl alloys under heavy ion irradiations, J. Nucl. Mater. 503 (2018) 250–262. https://doi.org/10.1016/j.jnucmat.2018.03.002.

[50] ORNL, Handbook on the Material Properties of FeCrAl alloys for Nuclear Power Production Applications, 2017.

[51] K.G. Field, M. Snead, Y. Yamamoto, B.A. Pint, K.A. Terrani, Materials properties of FeCrAl alloys for nuclear power production applications, (2017) 39.

[52] Y. Yamamoto, B.A. Pint, K.A. Terrani, K.G. Field, Y. Yang, L.L. Snead, Development and property evaluation of nuclear grade wrought FeCrAl fuel cladding for light water reactors, J. Nucl. Mater. 467 (2015) 703–716. https://doi.org/10.1016/j.jnucmat.2015.10.019.

[53] Y. He, J. Liu, S. Qiu, Z. Deng, Y. Yang, A. McLean, Microstructure and high temperature mechanical properties of as-cast FeCrAl alloys, Mater. Sci. Eng. A. 726 (2018) 56–63. https://doi.org/10.1016/j.msea.2018.04.039.

[54] Z. Chen, J. Cai, R. Liu, Y. Wang, Preliminary thermal hydraulic analysis of various accident tolerant fuels and claddings for control rod ejection accidents in LWRs, Nucl. Eng. Des. 331 (2018) 282–294. https://doi.org/10.1016/j.nucengdes.2018.03.007.

[55] Su G., M. Bucci, P. Sabharwall, Investigations on the Thermal-hydraulic Behavior of Accident Tolerant Fuel Cladding Materials. No. INL/EXT-19-56455-Rev000. Idaho National Lab. (INL), Idaho Falls, ID (United States), 2020.

[56] N.R. Brown, A.J. Wysocki, K.A. Terrani, A. Ali, M. Liu, E. Blandford, Survey of Thermal-Fluids Evaluation and Confirmatory Experimental Validation Requirements of Accident Tolerant Cladding Concepts with Focus on Boiling Heat Transfer Characteristics, Technical report for NEUP-DOE, June 2016.

[57] B. Zohuri, N. Fathi, Thermal-Hydraulic Analysis of Nuclear Reactors, 2015. https://doi.org/10.1007/978-3-319-17434-1.

[58] S.G. Kandlikar, A Theoretical Model to Predict Pool Boiling CHF Incorporating Effects of Contact Angle and Orientation, J. Heat Transfer. 123 (2001) 1071. https://doi.org/10.1115/1.1409265.

[59] J. Kim, S. Jun, R. Laksnarain, S.M. You, Effect of surface roughness on pool boiling heat transfer at a heated surface having moderate wettability, Int. J. Heat Mass Transf. 101 (2016) 992–1002. https://doi.org/10.1016/j.ijheatmasstransfer.2016.05.067.

[60] W.M. Rohsenow, A Method of Correlating Heat Transfer Data for Surface Boiling of Liquids, Trans. ASME. Vol.74 (n.d.) 969–976.

[61] C.C. Hsu, P.H. Chen, Surface wettability effects on critical heat flux of boiling heat transfer using nanoparticle coatings, Int. J. Heat Mass Transf. 55 (2012) 3713–3719.

https://doi.org/10.1016/j.ijheatmasstransfer.2012.03.003.

[62] N. Zuber, Hydrodynamic Aspects Of Boiling Heat Transfer (Thesis), (1959). https://doi.org/10.2172/4175511.

[63] A. Ali, H.G. Kim, K. Hattar, S. Briggs, D. Jun Park, J. Hwan Park, Y. Lee, Ion irradiation effects on Cr-coated zircaloy-4 surface wettability and pool boiling critical heat flux, Nucl. Eng. Des. 362 (2020) 110581. https://doi.org/10.1016/j.nucengdes.2020.110581.

[64] H.H. Son, G.H. Seo, U. Jeong, D.Y. Shin, S.J. Kim, Capillary wicking effect of a Cr-sputtered superhydrophilic surface on enhancement of pool boiling critical heat flux, Int. J. Heat Mass Transf. 113 (2017) 115–128. https://doi.org/10.1016/j.ijheatmasstransfer.2017.05.055.

[65] G.H. Seo, G. Jeun, S.J. Kim, Enhanced pool boiling critical heat flux with a FeCrAl layer fabricated by DC sputtering, Int. J. Heat Mass Transf. 102 (2016) 1293–1307. https://doi.org/10.1016/j.ijheatmasstransfer.2016.06.077.

[66] G.M. Son, K.M. Kim, I.C. Bang, Chromia coating with nanofluid deposition and sputtering for accident tolerance, CHF enhancement, Int. J. Heat Mass Transf. 118 (2018) 890–899. https://doi.org/10.1016/j.ijheatmasstransfer.2017.11.060.

[67] D.H. Kam, J.H. Lee, T. Lee, Y.H. Jeong, Critical heat flux for SiC- and Cr-coated plates under atmospheric condition, Ann. Nucl. Energy. 76 (2015) 335–342. https://doi.org/10.1016/j.anucene.2014.09.046.

[68] N. Kim, H.H. Son, S.J. Kim, Oxidation effect on pool boiling critical heat flux enhancement of Cr-coated surface for accident-tolerant fuel cladding application, Int. J. Heat Mass Transf. 144 (2019) 118655. https://doi.org/10.1016/j.ijheatmasstransfer.2019.118655.

[69] A.F. Ali, J.P. Gorton, N.R. Brown, K.A. Terrani, C.B. Jensen, Y. Lee, E.D. Blandford, Surface wettability and pool boiling Critical Heat Flux of Accident Tolerant Fuel cladding-FeCrAl alloys, Nucl. Eng. Des. 338 (2018) 218–231. https://doi.org/10.1016/j.nucengdes.2018.08.024.

[70] H. Hyun, Y. Sik, S. Joong, Experimental study of saturated pool boiling heat transfer with FeCrAl- and Cr-layered vertical tubes under atmospheric pressure, Int. J. Heat Mass Transf. 128 (2019) 418–430. https://doi.org/10.1016/j.ijheatmasstransfer.2018.09.013.

[71] H.J. Jo, H. Yeom, E. Gutierrez, K. Sridharan, M. Corradini, Evaluation of critical heat flux of ATF candidate coating materials in pool boiling, Nucl. Eng. Des. 354 (2019) 110166. https://doi.org/10.1016/j.nucengdes.2019.110166.

[72] S.K. Lee, M. Liu, N.R. Brown, K.A. Terrani, E.D. Blandford, H. Ban, C.B. Jensen, Y. Lee, Comparison of steady and transient flow boiling critical heat flux for FeCrAl accident tolerant fuel cladding alloy , Zircaloy , and Inconel, Int. J. Heat Mass Transf. 132 (2019) 643–654. https://doi.org/10.1016/j.ijheatmasstransfer.2018.11.141.

[73] K.G. Lee, W.K. In, H.G. Kim, Quenching experiment on Cr-alloy-coated cladding for accident-tolerant fuel in water pool under low and high subcooling conditions, Nucl. Eng. Des. 347 (2019) 10–19. https://doi.org/10.1016/j.nucengdes.2019.03.017.

[74] D. Lee, B. Elward, P. Brooks, R. Umretiya, J. Rojas Supervised, M. Bucci Supervised, R.B. Rebak, M. Anderson Supervised, Enhanced flow boiling heat transfer on chromium coated zircaloy-4 using cold spray technique for Accident Tolerant Fuel (ATF) materials, Appl. Therm. Eng. 185 (2020) 116347. https://doi.org/10.1016/j.applthermaleng.2020.116347.

[75] B. Elward, Critical heat flux and heat transfer performance of accident tolerant fuel cladding in atmospheric flow boiling, University of Wisconsin-Madison, 2020.

[76] ASTM International, Astm D 5725, 99 (1999) 1–7.

[77] R. Umretiya, D. Ginestro, S. Bilbao y Leon, J. Rojas, B. Elward, M. Anderson, R.B. Rebak, Surface characteristics of accident tolerant fuels cladding and their potential impact in critical heat flux, in: 18th Int. Top. Meet. Nucl. React. Therm. Hydraul. NURETH 2019, 2019.

[78] M. Flynn, International Standard, 2003 (2003).

[79] E2546-07, Standard Practice for Instrumented Indentation Testing, ASTM B. Stand. 1 (2007) 1–23. https://doi.org/10.1520/E2546-07.2.

[80] E.S. Gadelmawla, M.M. Koura, T.M.A. Maksoud, I.M. Elewa, H.H. Soliman, Roughness parameters, J. Mater. Process. Technol. 123 (2002) 133–145. https://doi.org/10.1016/S0924-0136(02)00060-2.

[81] K.Y. Law, Definitions for hydrophilicity, hydrophobicity, and superhydrophobicity: Getting the basics right, J. Phys. Chem. Lett. 5 (2014) 686–688. https://doi.org/10.1021/jz402762h.

[82] C. Angle, Surface Wetting, Springer International Publishing, (2015), 1-162, n.d. https://doi.org/10.1007/978-3-319-25214-8.

[83] K.J. Kubiak, M.C.T. Wilson, T.G. Mathia, P. Carval, Wettability versus roughness of engineering surfaces, 271 (2011) 523–528.

[84] R.W.L. Fong, T. Nitheanandan, C.D. Bullock, L.F. Slater, G.A. McRae, Effect of oxidation and fractal surface roughness on the wettability and critical heat flux of class-peened zirconium alloy tubes., Proc. 5th Int. Conf. Boil. Heat Transf. (2003).

[85] V. Belaud, S. Valette, G. Stremsdoerfer, M. Bigerelle, S. Benayoun, Wettability versus roughness: Multi-scales approach, Tribol. Int. 82 (2015) 343–349. https://doi.org/10.1016/j.triboint.2014.07.002.

[86] Y.J. Lim, Y. Oshida, C.J. Andres, M.T. Barco, Surface characterizations of variously treated titanium materials., Int. J. Oral Maxillofac. Implants. 16 (n.d.) 333–42. http://www.ncbi.nlm.nih.gov/pubmed/11432653.

[87] D.R. Baer, M.H. Engelhard, A.S. Lea, P. Nachimuthu, T.C. Droubay, J. Kim, B. Lee, C. Mathews, R.L. Opila, L. V. Saraf, W.F. Stickle, R.M. Wallace, B.S. Wright, Comparison of the sputter rates of oxide films relative to the sputter rate of SiO2, J. Vac. Sci. Technol. A Vacuum, Surfaces, Film. 28 (2010) 1060–1072. https://doi.org/10.1116/1.3456123.

[88] S.M. Rossnagel, J.R. Sites, X-ray photoelectron spectroscopy of ion beam sputter deposited SiO 2 , TiO 2 , and Ta 2 O 5, J. Vac. Sci. Technol. an Off. J. Am. Vac. Soc. 2 (1984) 376–379.

[89] A. Sathyamoorthy, W. Weisweiler, Studies of the sputter deposition of carbon, silicon and SiC films, Thin Solid Films. 87 (1982) 33–42. https://doi.org/10.1016/0040-6090(82)90568-5.

[90] L. Kalina, V. Bílek, M. Bušo, J. Koplík, J. Másilko, Thickness determination of corrosion layers on iron using XPS depth profiling, Mater. Tehnol. 52 (2018) 537–540. https://doi.org/10.17222/mit.2016.180.

[91] M.P. Seah, T.S. Nunney, Sputtering yields of compounds using argon ions, J. Phys. D. Appl. Phys. 43 (2010). https://doi.org/10.1088/0022-3727/43/25/253001.

[92] N.S. McIntyre, D.G. Zetaruk, X-ray Photoelectron Spectroscopic Studies of Iron Oxides, Anal. Chem. 49 (1977) 1521–1529. https://doi.org/10.1021/ac50019a016.

[93] A.M. Salvi, J.E. Castle, J.F. Watts, E. Desimoni, Peak fitting of the chromium 2p XPS spectrum, Appl. Surf. Sci. 90 (1995) 333–341. https://doi.org/10.1016/0169-4332(95)00168-9.

[94] D. Briggs, X-ray photoelectron spectroscopy (XPS), Handb. Adhes. Second Ed. (2005) 621–622. https://doi.org/10.1002/0470014229.ch22.

[95] A.P. Grosvenor, B.A. Kobe, M.C. Biesinger, N.S. McIntyre, Investigation of multiplet splitting of Fe 2p XPS spectra and bonding in iron compounds, Surf. Interface Anal. 36 (2004) 1564–1574. https://doi.org/10.1002/sia.1984.

[96] M.C. Biesinger, B.P. Payne, A.P. Grosvenor, L.W.M. Lau, A.R. Gerson, R.S.C. Smart, Resolving surface chemical states in XPS analysis of first row transition metals, oxides and hydroxides: Cr, Mn, Fe, Co and Ni, Appl. Surf. Sci. 257 (2011) 2717–2730. https://doi.org/10.1016/j.apsusc.2010.10.051.

[97] T. Hryniewicz, K. Rokosz, Analysis of XPS results of AISI 316L SS electropolished and magnetoelectropolished at varying conditions, Surf. Coatings Technol. 204 (2010) 2583–2592. https://doi.org/10.1016/j.surfcoat.2010.02.005.

[98] M. Digne, P. Sautet, P. Raybaud, H. Toulhoat, E. Artacho, Structure and stability of aluminum hydroxides: A theoretical study, J. Phys. Chem. B. 106 (2002) 5155–5162. https://doi.org/10.1021/jp014182a.

[99] V. Prysiazhnyi, Atmospheric Pressure Plasma Treatment and Following Aging Effect of Chromium Surfaces, J. Surf. Eng. Mater. Adv. Technol. 03 (2013) 138–145.

https://doi.org/10.4236/jsemat.2013.32018.

[100] J. Ejenstam, M. Thuvander, P. Olsson, F. Rave, P. Szakalos, Microstructural stability of Fe-Cr-Al alloys at 450-550 °C, J. Nucl. Mater. 457 (2015) 291–297. https://doi.org/10.1016/j.jnucmat.2014.11.101.

[101] W. Han, K. Yabuuchi, A. Kimura, S. Ukai, N. Oono, T. Kaito, T. Torimaru, S. Hayashi, Effect of Cr/Al contents on the 475ºC age-hardening in oxide dispersion strengthened ferritic steels, Nucl. Mater. Energy. 9 (2016) 610–615. https://doi.org/10.1016/j.nme.2016.05.015.

[102] G. Ryge, D.E. Foley, C.W. Fairhurst, Micro-indentation Hardness, in: Annu. Meet. Int. Assoc. Dent. Res., 1960.

[103] N.M. George, K. Terrani, J. Powers, A. Worrall, I. Maldonado, Neutronic analysis of candidate accident-tolerant cladding concepts in pressurized water reactors, Ann. Nucl. Energy. 75 (2015) 703–712. https://doi.org/10.1016/j.anucene.2014.09.005.

[104] W.D. Callister Jr, Materials Science and Engineering - An Introduction (5th ed.), 9th ed., Hoboken, NJ : Wiley, 2014. https://doi.org/10.1108/acmm.2000.12847aae.001.

[105] S. Pramanik, S. Suwas, Low-Density Steels: The Effect of Al Addition on Microstructure and Properties, Jom. 66 (2014) 1868–1876. https://doi.org/10.1007/s11837-014-1129-2.

[106] R. Elilarassi, G. Chandrasekaran, Effect of annealing on structural and optical properties of zinc oxide films, Mater. Chem. Phys. 121 (2010) 378–384. https://doi.org/10.1016/j.matchemphys.2010.01.053.

[107] D.J. Quesnel, M. Meshii, J.B. Cohen, Residual stresses in high strength low alloy steel during low cycle fatigue, Mater. Sci. Eng. 36 (1978) 207–215. https://doi.org/10.1016/0025-5416(78)90073-3.

[108] A.C. Vermeulen, E. Houtman, Determination of alignment errors in classical XRD residual stress methods, Mater. Sci. Forum. 347 (2000) 17–22. https://doi.org/10.4028/www.scientific.net/msf.347-349.17.

[109] R.B. Rebak, DE-NE0008221 GE Final Technical and Scientific Report, Oct 2014 - Sep 2018.